

# Synthesis and characterization of SnO<sub>2</sub> loaded on groundnut shell activated carbon and photocatalytic activity on MB dye under sunlight radiation

S. Ragupathy<sup>1</sup> · T. Sathya<sup>2</sup>

Received: 22 October 2015 / Accepted: 8 February 2016 / Published online: 13 February 2016  
© Springer Science+Business Media New York 2016

**Abstract** Tin oxide (SnO<sub>2</sub>) nanoparticles were synthesized and loaded on groundnut shell activated carbon (SnO<sub>2</sub>/GNSAC) using by a chemical precipitation method and its photocatalytic activity was evaluated by photodegradation of methylene blue under sunlight radiation. The synthesized products were characterized by X-ray diffraction analysis, diffusion reflectance spectra show the optical properties and confirmation made by photoluminescence, Fourier transform infrared spectroscopy, scanning electron microscopy with energy dispersive X-ray and nitrogen adsorption–desorption technique. The various experimental parameters like amount of catalyst, initial pH and contact time for efficient dye degradation of methylene blue were concerned in this study. In the photodegradation of methylene blue, a significant increase in the reaction rate was observed with SnO<sub>2</sub>/GNSAC under sunlight. This increase is due to the high migration efficiency of photoinduced electrons and the inhibition of charge–carrier recombination due to the electronic interaction between SnO<sub>2</sub> and GNSAC.

## 1 Introduction

Nowadays, semiconductor photocatalysts have been attracted widely attention since the environment pollution problems become seriously [1]. Various semiconductor

photocatalysts such as, ZnO, TiO<sub>2</sub>, CdS, ZrO<sub>2</sub> and SnO<sub>2</sub> [2–7] and etc., among these tin oxide (SnO<sub>2</sub>) is one of the most important n-type wide-band gap (3.6 eV) semiconductor nanoparticles. It has found many practical applications, mainly as gas sensor material, electrode dye-sensitized in solar cells, catalysts [8–10]. In order to increase the utilization efficiency of TiO<sub>2</sub> on solar energy, researchers do a lot of works from decreasing the forbidden band-width of TiO<sub>2</sub> and suppressing the recombination of electrons and holes [11]. At present, the modification methods mainly include surface sensitization, metal ion doping and non metal ion doping. Among these, non metal modification such as carbon modification can decrease the band gap energy of TiO<sub>2</sub>, which can improve its photocatalytic activity. Recently, an intense effort has been devoted to loading TiO<sub>2</sub> on different supports such as SnO<sub>2</sub> loaded on AC, MWNT@SnO<sub>2</sub> [12]. Especially, TiO<sub>2</sub> loaded on GNSAC has drawn great attention since the high adsorption capability of GNSAC can help to enrich organic substrate around the catalyst, promoting the pollutant transfer process and hence increasing the photocatalytic efficiency. The synergistic effect of adsorption by GNSAC and photocatalytic decomposition by TiO<sub>2</sub> has been observed in the degradation of organic pollutants [13]. Tin oxide nanoparticles have been synthesized through different chemical routes, such as co-precipitation, sol–gel, hydrothermal, solvothermal method [14–17] and etc., among these; chemical precipitation method for the synthesis of SnO<sub>2</sub> nanoparticles has a number of advantages such as, precise control over the stoichiometry, low temperature synthesis, high purity and high chemical homogeneity [18]. In this study, groundnut shell activated carbon synthesized from groundnut shell by chemical activation and its chemical precipitation method was used to synthesis SnO<sub>2</sub> nanoparticles and loaded on groundnut shell

✉ S. Ragupathy  
ragupathymc@gmail.com

<sup>1</sup> Department of Physics, Salem College of Engineering and Technology, Salem, Tamilnadu 636111, India

<sup>2</sup> Department of Physics, Arunai Engineering College, Thiruvannamalai, Tamilnadu 606603, India

activated carbon (SnO<sub>2</sub>/GNSAC) were well characterized and their photocatalytic degradation of methylene blue (MB) under sunlight radiation. The high photocatalytic performance of SnO<sub>2</sub>/GNSAC was discussed based on the electron transfer between SnO<sub>2</sub> and GNSAC.

## 2 Materials and methods

### 2.1 Chemicals

Tin (II) chloride dehydrate (SnCl<sub>2</sub> · H<sub>2</sub>O), oxalic acid dehydrate (C<sub>2</sub>H<sub>2</sub>O<sub>4</sub> · 2H<sub>2</sub>O), phosphoric acid (H<sub>3</sub>PO<sub>4</sub>), Sodium hydroxide (NaOH) and methylene blue (C<sub>16</sub>H<sub>18</sub>N<sub>3</sub>SCI) were purchased from Merck and SD Fine. All chemicals were used as received since they were of analytical reagent grade with 99 % purity. Double distilled water was used for all dilution and sample preparation.

### 2.2 Synthesis of groundnut shell activated carbon (GNSAC)

The groundnut shells (GNS) were collected from Panruti taluk, Cuddalore district, Tamilnadu, India. The GNS was first washed with double distilled water to ensure that all impurities were removed and then dried in an oven at 110 °C for 24 h. GNS was then ground and sieved to obtain precursors of particle size less than 2 mm. The precursors were impregnated in phosphoric acid (H<sub>3</sub>PO<sub>4</sub>) solution at an impregnation ratio of 1:1 (wt% ratio of H<sub>3</sub>PO<sub>4</sub>: GNS) and the mix was continuously stirred using a magnetic stirrer. The sample was then dried and activated by muffle furnace heating (at a rate of 20 °C/min) at 600 °C for 120 min [19]. After cooling down to room temperature, the product was washed sequentially with 0.1 M NaOH and double distilled water to remove residual minerals. The washed sample was dried at 110 °C for 6 h and cooled at room temperature to obtain the groundnut shell activated carbon (GNSAC).

### 2.3 Synthesis of SnO<sub>2</sub> nanoparticles and loaded on GNSAC (SnO<sub>2</sub>/GNSAC)

The preparation of SnO<sub>2</sub> nanoparticles from tin (II) chloride dehydrate (SnCl<sub>2</sub> · H<sub>2</sub>O) and oxalic acid dehydrate (C<sub>2</sub>H<sub>2</sub>O<sub>4</sub> · 2H<sub>2</sub>O), 0.5 M of tin (II) chloride dehydrate and 0.75 M oxalic acid dehydrate were mixed drop by drop to obtain SnO<sub>2</sub>. Then SnO<sub>2</sub> loaded on groundnut shell activated carbon catalyst was prepared by a similar method by adding 1 g of GNSAC. The entire mixture was stirred magnetically at 70 °C until a white precipitate was formed. The obtained dispersions were purified by dialysis against double distilled water and ethanol several times to remove

impurities. The yield product was dried in a hot air oven at 100 °C for 6 h to evaporate water and organic material. Finally, the product was annealed in a muffle furnace at 400 °C for 2 h to obtain SnO<sub>2</sub> and SnO<sub>2</sub>/GNSAC.

### 2.4 Characterization

The crystalline phase and particle size of SnO<sub>2</sub> and loaded on groundnut shell activated carbon were analyzed by X-ray diffraction (XRD) measurement which was carried out at room temperature by using the X'PERT-PRO diffractometer system [scan step of 0.05° (2θ), counting time of 10.16 s per data point] equipped with a Cu tube for generating Cu Kα radiation (k = 1.5406 Å); as an incident beam in the 2-theta mode over the range of 10°–80°, operated at 40 kV and 30 mA. The band-gap energy was measured at wavelengths in the range of 200–800 nm by UV–Vis–NIR spectrophotometer (Varian/Carry 5000) equipped with an integrating sphere and the baseline correction was performed using a calibrated reference sample of powdered barium sulfate (BaSO<sub>4</sub>). The photoluminescence (PL) emission spectra of the samples were recorded with a spectrofluorometer (Jobin–Yvon, FLUOROLOG-FL3-11). The functional groups were determined by a SHIMADZU-8400 Fourier-transform infra-red spectrometer in which the IR spectra were recorded by diluting the milled powders in KBr and the wavelength between 4000 and 400 cm<sup>-1</sup> was used to assess the presence of functional groups in SnO<sub>2</sub> and loaded on GNSAC. The morphology of the products was explored using scanning electron microscope JEOL: JSM-5610LV equipped with energy dispersive spectrometer (Bruker) at an accelerating voltage of 20 kV. The BET measurements were recorded using Micromeritics ASAP 210 apparatus. The UV–Vis absorption measurements of the products during photocatalytic measurements were recorded in the wavelength range of 400–800 nm using a Shimadzu UV1800 spectrometer.

### 2.5 Photocatalytic activity experiment

Photocatalytic activity of SnO<sub>2</sub> and loaded on GNSAC was evaluated by studying photodegradation of MB dye solution under sunlight radiation. The optimum quantities of SnO<sub>2</sub> (0.015 g/L) were taken in separate open borosilicate glasses of 250 mL capacity. 100 mL of dye solution of initial concentration (20 mg/L) were then added to those vessels and the contents were stirred keeping irradiated under sunlight. All the experiments were conducted between 11.00 am and 02.00 pm under direct sunlight and the solar intensity (1250 × 100 Lu ± 100) was almost constant. After predetermined time intervals, adequate quantity of solutions were taken out and centrifuged (Remi centrifuge, Model No: C-85414 with 3000 rpm). The

concentration of dye in supernatant was analyzed using a Shimadzu UV1800 spectrophotometer by measuring the absorbance at respective  $\lambda_{\max}$  of 664 nm. The percentage of degradation of dye was calculated from the following equation [20].

$$\%D = \frac{C_o - C_t}{C_o} \times 100 \quad (1)$$

where  $C_o$  is the initial concentration of MB dye solutions (mg/L),  $C_t$  is the concentration of dye after irradiation after selected time interval (mg/L). The same procedure was adopted for SnO<sub>2</sub> loaded on GNSAC.

### 3 Results and discussion

#### 3.1 XRD analysis

The XRD spectra of GNSAC, SnO<sub>2</sub> and loaded on GNSAC are shown in Fig. 1. The XRD spectra of GNSAC in shows two broad peaks which can be indexed to (002) and (100) diffraction plane. In exhibits two broad peaks and the absence of sharp peak reveals a predominantly amorphous structure. All diffraction peaks are indexed to the tetragonal structure of SnO<sub>2</sub> with lattice parameters comparable to that of the JCPDS card (88-0287). The intensity of the diffraction peaks shows a reduced with SnO<sub>2</sub> loaded on GNSAC. The average crystalline sizes of the synthesized samples were calculated using the Debye–Scherer formula [21].

$$D = \frac{K\lambda}{\beta \cos \theta} \quad (2)$$

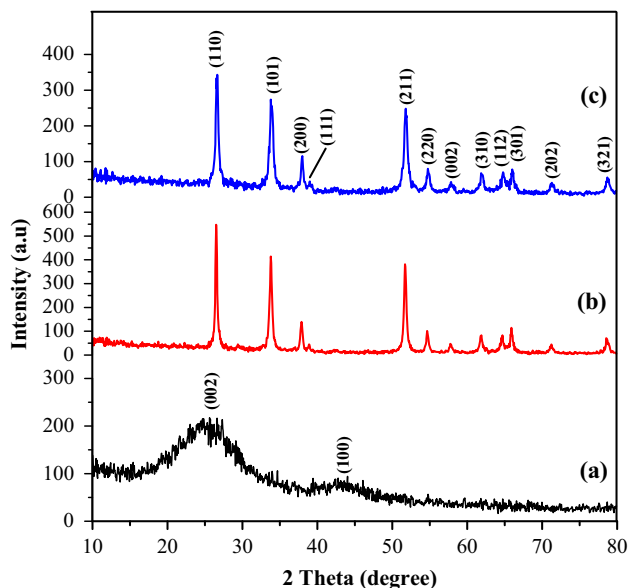


**Fig. 1** XRD patterns of *a* GNSAC, *b* SnO<sub>2</sub> and *c* SnO<sub>2</sub>/GNSAC

where  $D$  is the average crystallite diameter (Å),  $K$  is the Scherrer's constant (0.9),  $\lambda$  is the wavelength (1.5406 Å),  $\beta$  is the full width at half maximum and  $\theta$  is the Bragg's angle. The lattice parameters 'a' and 'c' for the tetragonal structure ( $a = b \neq c$ ,  $\alpha = \beta = \gamma = 90^\circ$ ) can be calculated by the following equation,

$$\sin^2 \theta = \frac{\lambda^2(h^2 + k^2)}{4a^2} + \frac{\lambda^2(l^2)}{4c^2} \quad (3)$$

where  $h$ ,  $k$  and  $l$  are the miller indices of the peaks. From the values of 'a' and 'c', the unit cell volume ( $V$ ) of the products is given by the formula  $V = a^2c$  [22]. The calculated crystallite size, lattice parameters and unit-cell volume for SnO<sub>2</sub> and SnO<sub>2</sub>/GNSAC are given in Table 1. As shown in the table, it can be observed that the average crystallite size of SnO<sub>2</sub> is around 24.06 nm and SnO<sub>2</sub> loading on groundnut shell activated carbon, the particle size reduced to 18.12 nm [23]. This drop could be explained by SnO<sub>2</sub> form and settles in the micro and mesopores of the groundnut shell activated carbon which limits its growth. It is well know that smaller sized particles could lead to larger surface area, which would be beneficial for increasing the photocatalytic activity.

#### 3.2 Ultra violet-diffuse reflectance spectra (UV-DRS)

The diffuse reflectance spectra of SnO<sub>2</sub> and SnO<sub>2</sub>/GNSAC recorded 300–800 nm ranges are shown in Fig. 2. The band gap energies ( $E_g$ ) of modified SnO<sub>2</sub> and SnO<sub>2</sub>/GNSAC are obtained from the wavelength values corresponding to the intersection point of the vertical and horizontal parts of the spectra, using the equation [24].

$$E_g = \frac{hc}{\lambda} \text{eV} \quad (4)$$

where  $E_g$  is the band gap energy (eV),  $h$  is the Planck's constant ( $6.626 \times 10^{-34}$  Js),  $c$  is the light velocity ( $3 \times 10^8$  m/s) and  $\lambda$  is the Wavelength (nm). The band gap energy ( $E_g$ ) calculated from SnO<sub>2</sub> and SnO<sub>2</sub>/GNSAC is 3.75 and 3.64 eV. Since the band gap energies are higher than the bulk value of SnO<sub>2</sub> (3.6 eV). The observed red shift and the decreased band gap indicate that the band structure SnO<sub>2</sub>/GNSAC. These lower band gap values are favorable to photocatalytic activity.

#### 3.3 Photoluminescence (PL)

The PL properties of as-prepared SnO<sub>2</sub> and SnO<sub>2</sub>/GNSAC were studied at room temperature (Fig. 3). From the PL spectra, it is predicted that the SnO<sub>2</sub> exhibits five emission peaks two at UV region (342 and 400 nm) and other three at visible region (436, 467 and 481 nm). The spectra are

**Table 1** XRD derived parameters of SnO<sub>2</sub> and SnO<sub>2</sub>/GNSAC

Samples	Particle size (nm)	Lattice parameters (Å)		Volume (Å <sup>3</sup> )
		a	c	
SnO <sub>2</sub>	24.06	4.745	3.188	71.782
SnO <sub>2</sub> /GNSAC	18.12	4.735	3.184	71.658

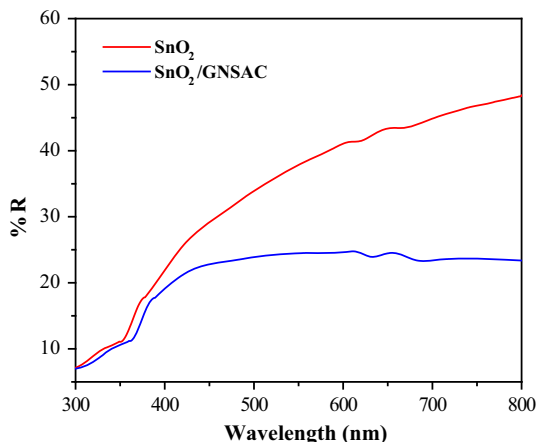


**Fig. 2** UV-Vis-diffuse reflectance spectra of SnO<sub>2</sub> and SnO<sub>2</sub>/GNSAC

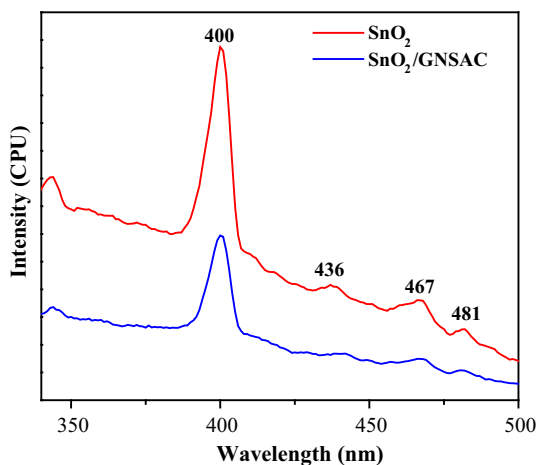


**Fig. 3** PL emission spectra of SnO<sub>2</sub> and SnO<sub>2</sub>/GNSAC

broad band emission in the range of 385–407 nm for SnO<sub>2</sub> and SnO<sub>2</sub>/GNSAC. The intensity of the PL spectra decreased in the following order for the photocatalysts; SnO<sub>2</sub> and SnO<sub>2</sub>/GNSAC. The possible mechanism behind the quenching of UV emission and enhancement of visible emissions is explained as follows. For SnO<sub>2</sub>/GNSAC sample, with the SnO<sub>2</sub> loaded on groundnut shell activated carbon content, the intensity of UV and visible band is found to decrease as a result of the inhibition of recombination of the excitons. Generally the lower PL intensity suggest the lower the recombination rate of photogenerated

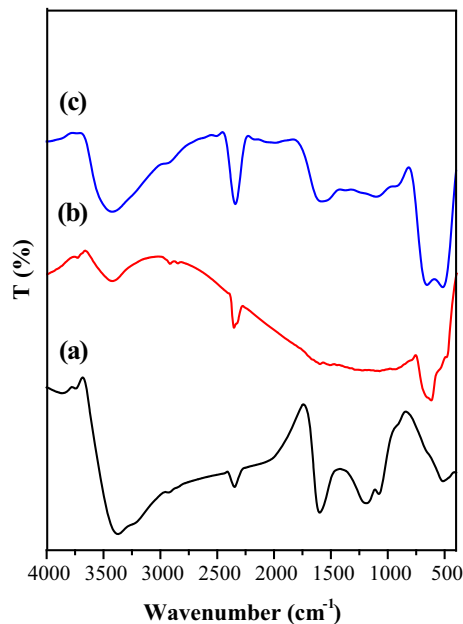


**Fig. 4** FT-IR spectra of a GNSAC, b SnO<sub>2</sub> and c SnO<sub>2</sub>/GNSAC

electron–hole pairs, which leads to the higher photocatalytic activity has been reported by Wang et al. [12]. Therefore, the low PL intensity for SnO<sub>2</sub>/GNSAC indicates that the photocatalytic activities of SnO<sub>2</sub> may be improved due to the interactions between the excited electron of SnO<sub>2</sub> nanoparticles and the GNSAC.

### 3.4 Functional group analysis

The FT-IR spectra of the GNSAC, SnO<sub>2</sub> and SnO<sub>2</sub>/GNSAC are shown in Fig. 4. The spectra of GNSAC display absorption bands at 3373.50, 2931, 1599 and 1188.15 2931 cm<sup>-1</sup>. The spectra of GNSAC broad band at 3373.50 cm<sup>-1</sup> is due to the O–H stretching mode of hydroxyl group. The sharp peak located at 2931 cm<sup>-1</sup> corresponding to aliphatic C–H stretching vibrations, while the band at 1599 cm<sup>-1</sup> to C=C stretching of aromatic group. The peak at 1188.15 cm<sup>-1</sup> is assigned to the stretching vibration P–O–C (aromatic) linkage and P=OOH. The spectra of both SnO<sub>2</sub> and SnO<sub>2</sub>/GNSAC exhibit adsorption bands located at 3423.65 cm<sup>-1</sup> is owing to the vibration of O–H and the band located at 1614.42 cm<sup>-1</sup> is due to the H–O–H vibrating mode of the

absorbed water [25]. The band at  $623.01$  and  $489.92\text{ cm}^{-1}$  is attributed to the Sn–O stretching vibrations and the O–Sn–O blending vibration in  $\text{SnO}_2$  [18].

### 3.5 Morphological analysis

SEM images of  $\text{SnO}_2$  and  $\text{SnO}_2/\text{GNSAC}$  are shown in Fig. 5a, b along with their EDS analyses.  $\text{SnO}_2$  is observed to exhibit spherical morphology.  $\text{SnO}_2/\text{GNSAC}$  exhibits a rough porous surface resulting from the growth of  $\text{SnO}_2$  nanoparticles on GNSAC surface.

### 3.6 Nitrogen adsorption–desorption isotherms

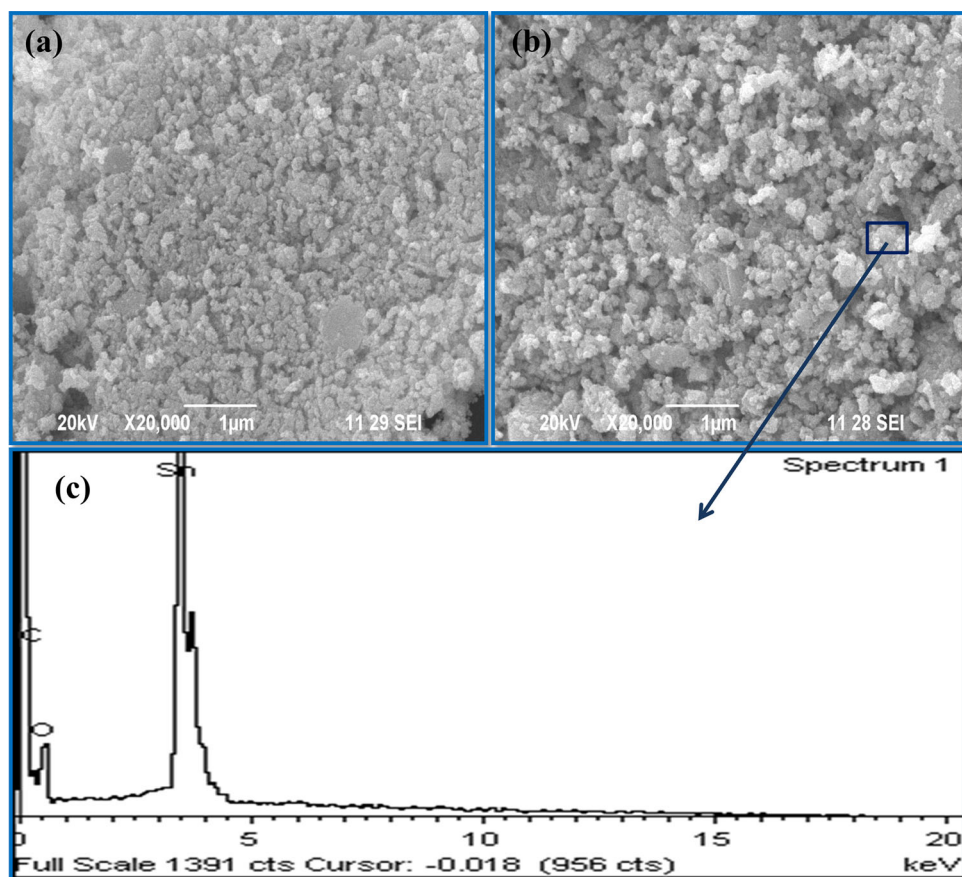
The surface textures of  $\text{SnO}_2$  and  $\text{SnO}_2/\text{GNSAC}$  were determined by nitrogen adsorption and desorption isotherms, as shown in Fig. 6a, b, the isotherms exhibit a type IV  $H_3$  hysteresis loop with mesopores structure. The surface area of  $\text{SnO}_2$  determined from BET measurement is  $20.80\text{ m}^2/\text{g}$  [26], Whereas, it is increased to  $236.50\text{ m}^2/\text{g}$  for  $\text{SnO}_2$  loaded on GNSAC. The pore size distribution curves (insets of Fig. 6a, b) reveal the pore volume of  $\text{SnO}_2$  and  $\text{SnO}_2$  loaded on GNSAC as  $0.26$  and  $0.30\text{ cm}^3/\text{g}$ , respectively. The higher surface area of the  $\text{SnO}_2$  loaded on

GNSAC recommends its usage in enhanced photocatalytic activity.

### 3.7 Effect of catalyst dosage

The effect of catalyst dosage on degradation of methylene blue dye is illustrated in Fig. 7, respectively. The experiments were run with varying catalyst dosage from  $0.005$  to  $0.025\text{ g/L}$  in  $20\text{ mg/L}$  solution of MB for  $120\text{ min}$  under sunlight. The percent removal of the dye reached their maximum at  $0.015\text{ g/L}$  of  $\text{SnO}_2$  and  $\text{SnO}_2/\text{GNSAC}$  respectively and then decreased. It should be pointed out that the catalyst loading affects number of active site on the photocatalyst and the penetration of radiation through the suspension. As the catalyst loading increases the percent removal of MB decreases due to the enhancement of light reflectance by GNSAC. The number of sites increases but the penetration of radiation decreases due to shielding effect [23]. In our study, the optimum value of catalyst loading for  $\text{SnO}_2$  and  $\text{SnO}_2/\text{GNSAC}$  were  $0.015\text{ g/L}$  under sunlight corresponding MB removals over  $\text{SnO}_2$  and  $\text{SnO}_2/\text{GNSAC}$  were  $71.51$  and  $97\%$  respectively under sunlight within  $120\text{ min}$  constant time and pH 5 for  $\text{SnO}_2$  and  $\text{SnO}_2/\text{GNSAC}$ .

**Fig. 5** SEM images of **a**  $\text{SnO}_2$  and **b**  $\text{SnO}_2/\text{GNSAC}$  corresponding EDS spectra (c)



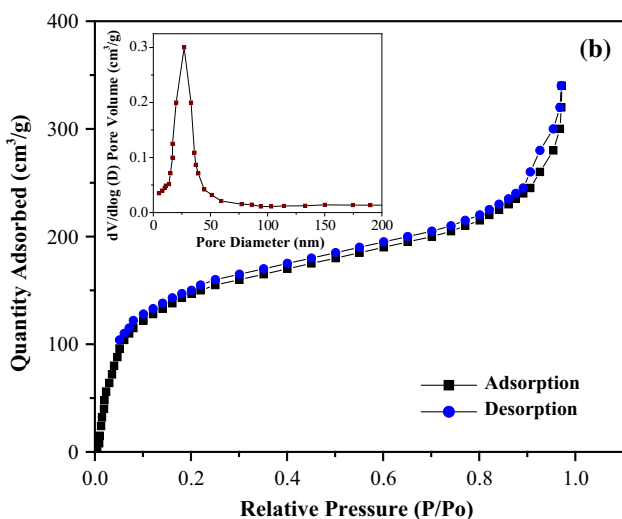
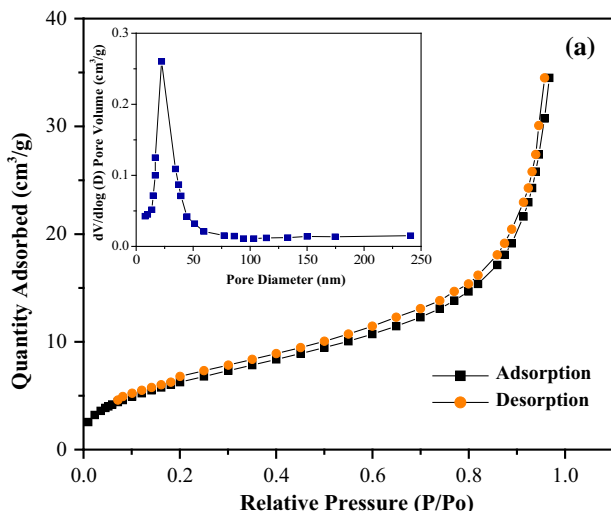


**Fig. 6** **a** Nitrogen adsorption and desorption isotherms and the corresponding pore size distribution curve (*inset*) of SnO<sub>2</sub> nanoparticles, **b** nitrogen adsorption and desorption isotherms and the corresponding pore size distribution curve (*inset*) of SnO<sub>2</sub>/GNSAC

### 3.8 Effect of pH

The effect of initial pH (2–9) on 20 mg/L of MB removal at room temperature using 0.015 g/L (SnO<sub>2</sub>/GNSAC only) of present adsorbent was investigated for 120 min. Variation of MB removal with pH is shown in Fig. 8. The results show that the MB removal increased following rising initial pH 2–4 and in the pH range of 6–8 decreased. It may be seen from the figure that maximum MB removal was obtained at pH 5. Hence the higher degradation efficiency is due to the strong adsorption of MB on the SnO<sub>2</sub>/GNSAC. The surface charge properties of SnO<sub>2</sub>/GNSAC changed with pH. The point of zero charge (pzc) for SnO<sub>2</sub>/GNSAC is at pH ≈ 6.5. The SnO<sub>2</sub>/GNSAC surface is positively charged in acid solution (pH < pzc) and negatively

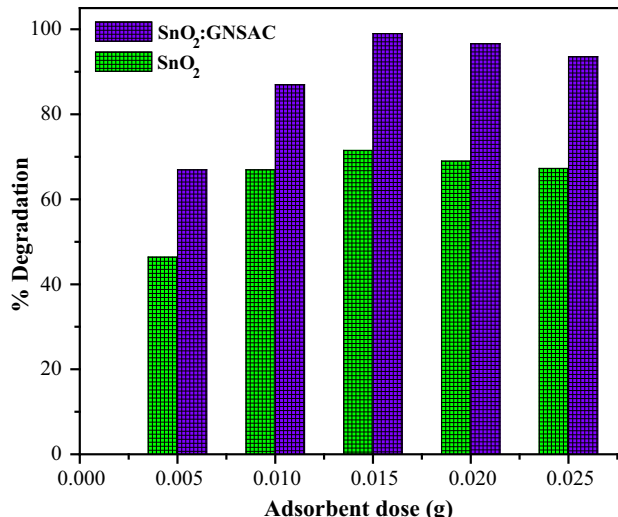


**Fig. 7** Effect of catalyst dosage on photocatalytic degradation of MB dye in presence of SnO<sub>2</sub> and SnO<sub>2</sub>/GNSAC

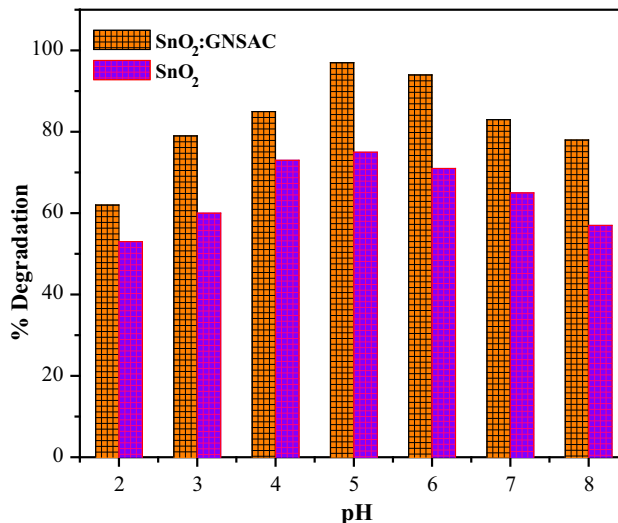


**Fig. 8** Effect of pH on photocatalytic degradation of MB dye in presence of SnO<sub>2</sub> and SnO<sub>2</sub>/GNSAC

charged in basic solution (pH > pzc). At low pH leads to an increase, the number of positive charged by adsorbing dye. As the SnO<sub>2</sub>/GNSAC surface is positively charged at pH 5, a significantly strong electrostatic attraction appears between the positively charged SnO<sub>2</sub>/GNSAC surface and dye molecule leading to maximum adsorption of dye. As the pH of the system increases, the number of negatively charged site on the SnO<sub>2</sub>/GNSAC does not favor the adsorption of dye molecules due to the electrostatic repulsion, then the adsorption process will decrease significantly.

### 3.9 Effect of contact time

Effect of contact time of catalysts SnO<sub>2</sub> and SnO<sub>2</sub>/GNSAC on photocatalytic degradation of MB are shown in Fig. 9. The UV–visible spectra of MB dye solution after different intervals of photodegradation in presence of SnO<sub>2</sub> and SnO<sub>2</sub>/GNSAC are shown in Fig. 10a, b. Contact time experiments were run with optimum catalyst loading of SnO<sub>2</sub> and SnO<sub>2</sub>/GNSAC (0.015 g/L) in 20 mg/L dye solution at constant solution pH of 5, for 120 min under sunlight. The photocatalytic efficiency of catalysts was evaluated in terms of percentage of dye degrade using Eq. (1). It can be seen that the increase in the contact time on photodegradation efficiency of naked SnO<sub>2</sub> reached 77 % respectively after 120 min irradiation time. In case SnO<sub>2</sub>/GNSAC, the efficiency of MB reached 97 % after same irradiation time. This fact is in agreement with the surface area is higher for the SnO<sub>2</sub>/GNSAC than for the SnO<sub>2</sub>. This result indicated that there is an interaction between GNSAC and SnO<sub>2</sub>, the size of the SnO<sub>2</sub>/GNSAC get smaller and the surface area increased.

### 3.10 Kinetic studies

The rate constant values for dye degradation for the catalysts were calculated using first order rate equation [27].

$$\ln \frac{C_0}{C_t} = kt \quad (5)$$

where  $k$  is the first order rate constant. Figure 11 shows the plots depicting a linear relationship between  $\ln \frac{C_0}{C_t}$  and time for all the samples and from the slope of the graph, rate constant and regression coefficient ( $R^2$ ) values were calculated and summarized in Table 2. It can be seen from

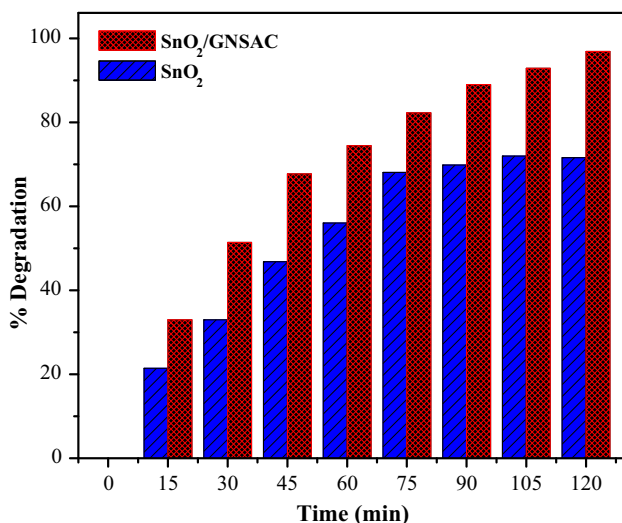


**Fig. 9** Effect of MB dye degradation by SnO<sub>2</sub> and SnO<sub>2</sub>/GNSAC

table that the rate constant value for SnO<sub>2</sub> was found to be 0.0093 min<sup>-1</sup>, while for SnO<sub>2</sub> loaded on GNSAC, it was increased to 0.0286 min<sup>-1</sup>. The increased rate constant ( $k$ ) value of SnO<sub>2</sub>/GNSAC suggests the excellent photocatalytic activity of SnO<sub>2</sub> loaded on GNSAC.

### 3.11 Photodegradation mechanism

The photocatalytic activity is based on the reactive nature of an electron–hole pair generated in semiconductor nanoparticles under illumination by light of energy greater than the semiconductor band gap electron is excited to the conduction band gap and electron in the conduction band migrates to the particles surface. It no recombination takes place, these charge carries can react with O<sub>2</sub> to generate •O<sub>2</sub> and the holes theoretically migrate to the surface and react with OH<sup>-</sup> or H<sub>2</sub>O to generate OH•, these radicals can

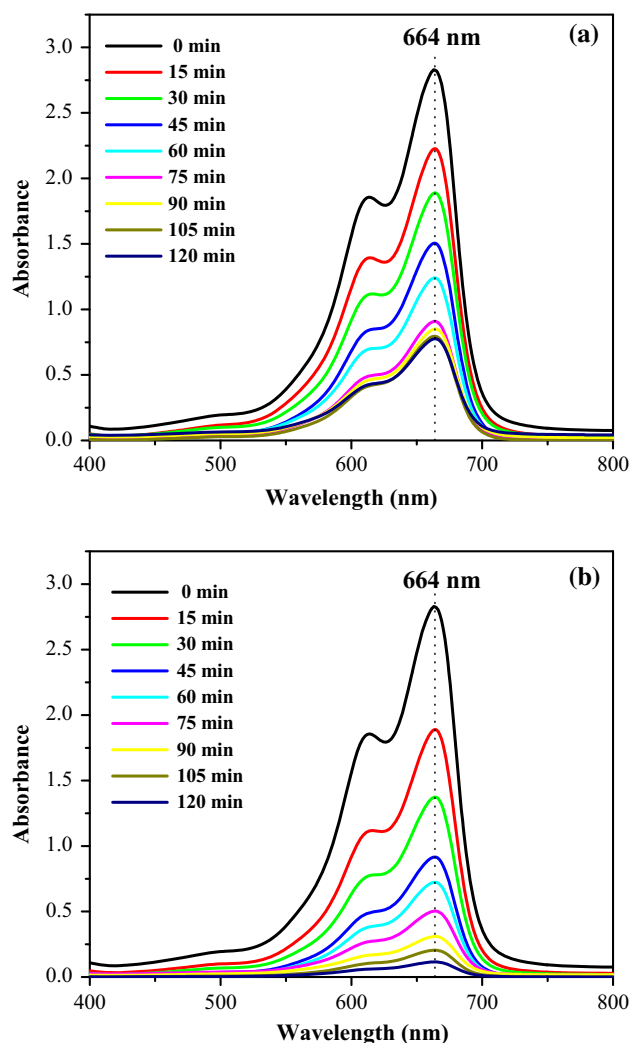


**Fig. 10** **a** UV–Vis absorption spectra of MB solution in the presence of SnO<sub>2</sub> at different intervals. **b** UV–Vis absorption spectra of MB solution in the presence of SnO<sub>2</sub>/GNSAC at different intervals

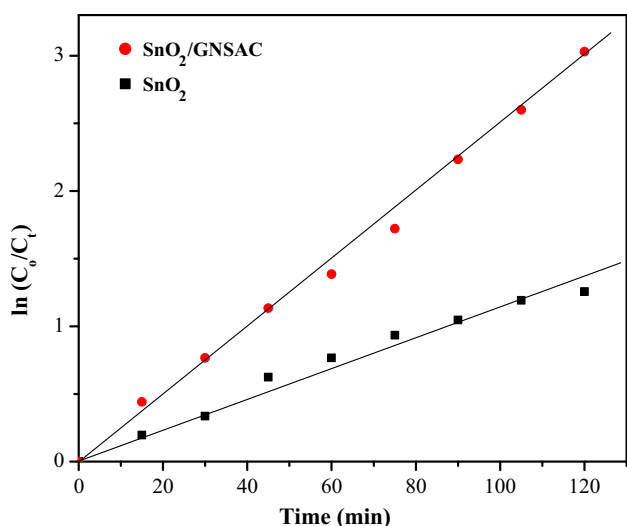


**Fig. 11** Kinetic study of photodegradation of MB in the presence of SnO<sub>2</sub> and SnO<sub>2</sub>/GNSAC

**Table 2** The rate constants and linear regression coefficients of MB photodegradation

Samples	Rate constant (min <sup>-1</sup> )	R <sup>2</sup>
SnO <sub>2</sub>	0.0093	0.976
SnO <sub>2</sub> /GNSAC	0.0286	0.985

react with adsorbed organic pollutants. The reactions can be expressed as follows;

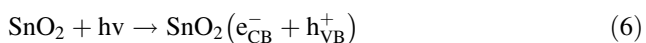


**Fig. 12** Illustration of Photodegradation mechanism of MB dye over SnO<sub>2</sub>/GNSAC

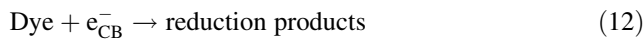
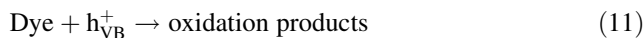
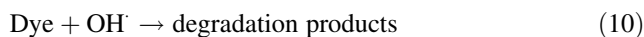
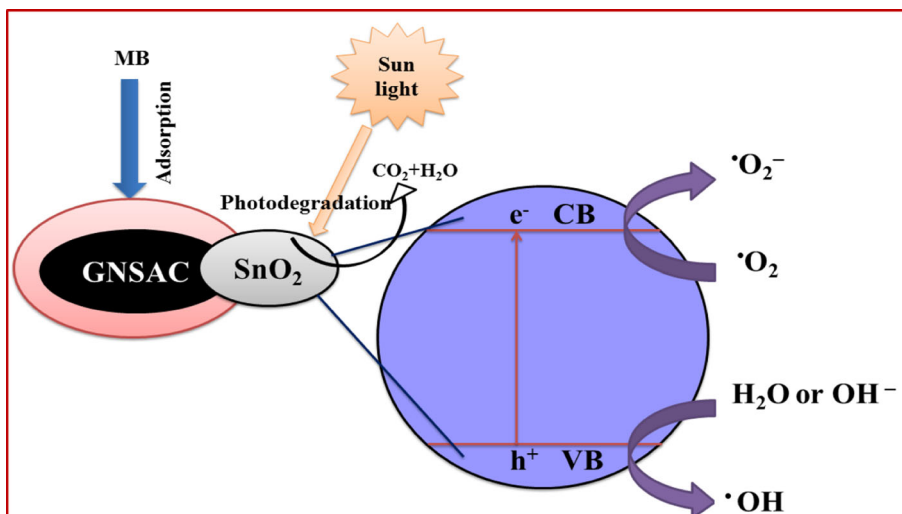


Figure 12 depicts possible structure of SnO<sub>2</sub> loaded on GNSAC with adsorption capacity and photocatalytic activity. As mentioned in the previous section a large amount of SnO<sub>2</sub> will be exposed on the surface of GNSAC by long activation time. As a result, active site available on the surface of GNSAC will increase. This may also contribute to the high photocatalytic activity of SnO<sub>2</sub>/GNSAC. In such a case, there seems to exist a synergistic effect in the composite due to the combination of the adsorption capacity of the GNSAC and the photocatalytic of SnO<sub>2</sub> [28].

### 4 Conclusions

In summary, SnO<sub>2</sub> and SnO<sub>2</sub>/GNSAC were successfully synthesized using co precipitation method. The XRD analyses reveal that the prepared SnO<sub>2</sub> were attributed to the tetragonal system and average crystallite size got decreased when supported on GNSAC. Decrease of photoluminescence intensity reveals the suppression of electron–hole recombination by the SnO<sub>2</sub> loaded on GNSAC. The BET analysis confirms the increase in the surface area of SnO<sub>2</sub> loaded on GNSAC. The experiments revealed that the photocatalytic oxidation of MB aqueous solution is more effective in SnO<sub>2</sub>/GNSAC than naked SnO<sub>2</sub>. About 97 % degradation of MB was observed with SnO<sub>2</sub>/GNSAC in comparison to 77 % degradation of MB with naked SnO<sub>2</sub> using sunlight respectively within 120 min irradiation time and the same amount of catalysts. The higher photocatalytic oxidation efficiency of SnO<sub>2</sub>/GNSAC at pH



5 is due to synergistic effect of GNSAC. The kinetic rate constant of degradation is higher in the presence of SnO<sub>2</sub>/GNSAC.

**Acknowledgments** The authors wish to thank Dr. R.A. Sankaran, The Principal, Salem College of Engineering and Technology, Salem, Tamilnadu, India, for having provided the necessary facilities to carry out this work. The authors also thank Centralized Instrumentation and Services Laboratory (CISL), Annamalai University and Sophisticated Analytical Instrumentation Facility (SAIF), Cochin, for providing their analytical instrument facilities.

## References

1. K. Rajeshwar, C.R. Chenthamarakshan, S. Goeringer, M. Djukic, *Pure Appl. Chem.* **73**, 1849–1860 (2001)
2. Y.H. Jang, S.T. Kochuveedu, M.A. Cha, Y.J. Jang, J.Y. Lee, J. Lee, J.Y. Kim, D.Y. Ryu, D.H. Kim, *J. Colloid Interface Sci.* **345**, 125–130 (2010)
3. A. Ajmal, I. Majeed, R.N. Malik, H. Idriss, M.A. Nadeem, *RSC Adv.* **4**, 37003–37026 (2014)
4. S.K. Tang, T.T. Teng, A.F.M. Alkarkhi, Z. Li, *APCBEE Procedia* **1**, 110–115 (2012)
5. A. Nezamzadeh-Ejhieh, Z. Banan, *Desalination* **284**, 157–166 (2012)
6. H. Matsui, N. Bandou, S. Karuppuchamy, M.A. Hassan, M. Yoshihara, *Ceram. Int.* **38**, 1605–1610 (2012)
7. X. Jia, Y. Liu, X. Wu, Z. Zhang, *Appl. Surf. Sci.* **311**, 609–613 (2014)
8. C. Li, Z. Yu, S. Fang, S. Wu, Y. Gui, R. Chen, *J. Phys.* **152**, 012033 (2009)
9. G. Shang, J. Wu, S. Tang, L. Liu, X. Zhang, *J. Phys. Chem. C* **117**, 4345–4350 (2013)
10. L. Neftali, V. Carreno, M.R. Nunes, I.T.S. Garcia, M.O. Orlandi, H.V. Fajardo, E. Longo, *J. Nanopart. Res.* **11**, 955–963 (2009)
11. Z.L. Ma, G.F. Huang, D.S. Xu, M.G. Xia, W.Q. Huang, Y. Tian, *Mater. Lett.* **108**, 37–40 (2013)
12. N. Wang, J. Xu, L. Guan, *Mater. Res. Bull.* **46**, 1372–1376 (2011)
13. S. Ragupathy, K. Raghu, *Int. J. Cur. Res.* **6**, 8427–8432 (2014)
14. K. Gopinadhan, S.C. Kashyap, D.K. Pandya, S. Chaudharya, *J. Appl. Phys.* **102**, 113513 (2007)
15. A. Azam, A.S. Ahmed, S.S. Habib, A.H. Naqvi, *J. Alloys Compd.* **523**, 83–87 (2012)
16. H. Zhu, D. Yang, G. Yu, H. Zhang, K. Yao, *Nanotechnology* **17**, 2386 (2006)
17. L. Xia, B. Yang, Z. Fu, Y. Yang, H. Yan, Y. Xu, *Mater. Lett.* **61**, 1214–1217 (2007)
18. M. Aliahmad, M. Dehbashi, *J. Energy Environ.* **4**, 49–52 (2013)
19. H. Cherifia, B. Fatihab, H. Salah, *Appl. Surf. Sci.* **282**, 52–59 (2013)
20. Mi-Hwa Baek, Ji-Won Yoon, Ji-Sook Hong, Jeong-Kwon Suh, *Appl. Catal. A* **450**, 222–229 (2013)
21. X. Wang, Y. Liu, Z. Hu, Y. Chen, W. Liu, G. Zhao, *J. Hazard. Mater.* **169**, 1061–1067 (2009)
22. R. Chauhan, A. Kumar, R.P. Chaudhary, *J. Sol-Gel. Sci. Technol.* **61**, 585–591 (2012)
23. T.S. Jamil, M.Y. Ghaly, N.A. Fathy, T.A. Abd el-halim, L. Osterlund, *Sep. Purif. Technol.* **98**, 270–279 (2012)
24. W. Zhao, Z. Bai, A. Ren, B. Guo, C. Wu, *Appl. Surf. Sci.* **256**, 3493–3498 (2010)
25. N. Rajesh, J.C. Kannan, T. Krishnakumar, S.G. Leonardi, G. Neri, *Sens. Actuators B* **194**, 96–104 (2014)
26. N. Shanmugam, T. Sathya, G. Viruthagiri, C. Kalyanasundaram, R. Gobi, S. Ragupathy, *Appl. Surf. Sci.* **360**, 283–290 (2016)
27. J. Matos, J. Laine, J.M. Herrmann, *Appl. Catal. B* **18**, 281–291 (1998)
28. S. Ragupathy, K. Raghu, P. Prabu, *Spectrochim. Acta Part A* **138**, 314–320 (2015)